Research Article

Tuning the dopant (Zn^{2+}) composition for uniform mesoporous Zn–CuS nanoflower via hydrothermal approach as a novel electrode material for high-rate supercapacitor

Surekha Podili[1] · D. Geetha[1] · P. S. Ramesh[2]

© Springer Nature Switzerland AG 2020

Abstract

We proposed a facile strategy to synthesize porous zinc-doped copper sulfide (Zn–CuS) nanoflowers using a cationic surfactant (CTAB) by hydrothermal route. The end product is used as electrode material in supercapacitor in KOH as electrolyte. Initially it is found that inorganic dopant (Zn^{2+}) plays a vital role in controlling or modifying the morphology of CuS which has resulted in the newer materials exhibiting multi-functional, high-performance stabilizer character further than what traditional single nanomaterials possess. Morphological analysis illustrates flower-like structures that the size of Zn–CuS nanostructure is about 14–20 nm. When utilized as an electroactive material for electrochemical capacitors, the Zn–CuS electrode delivers a specific capacitance (C_s) 826.31 Fg^{-1} at $5 mAcm^{-2}$, which is higher than the CuS electrode 328.26 Fg^{-1} at $5 mAcm^{-2}$. The outstanding electrochemical behavior is essentially by reason of the porous nature of synthesized nanostructures, which gives quick diffusion pathway to electronic and ionic transport on electrode and electrolyte interfaces. This exploration work affirms that the Zn–CuS electrode can serve as more attractive material for supercapacitive applications.

Keywords Mesoporous Zn–CuS · Cationic surfactant · Nanoflower · Electrode material · Supercapacitor

1 Introduction

With the expanding utilization of electronic devices and vehicles, explore research have been made to investigate superior storage frameworks. Among these charge storage systems, SCs have been shown to be most favorable power sources attributable to their outstandingly high energy density, small charge and discharge times, and ultra-long cycle life [1–5]. Be that as it may, the energy density of commercially used SCs is about 5 wh kg^{-1}, which is lower than other energy storage devices like Li-ion batteries [6]. The charge in SCs is stored by the electro active materials. So it is attractive and vital to design superior electrode materials so as to advance the energy density of SCs.

Carbon-based materials, transition metal oxides/hydroxide, and conducting polymers are among the most seriously investigated SC's electode materials. Carbon materials show low capacitance because of their surface predominant EDLCs mechanism [7–9]. Transition metal oxides show higher capacitance inferable from their redox-response improved energy storage system. Be that as it may, these materials have poor electrochemical strength, a reality that has, to a great extent constrained their far reaching applications in SCs. Therefore, it is vital to grow new electrode materials with attractive supercpacitor properties, such as high electrical conductivity, porous structure, substantial capacitors, and great electrochemical stability.

✉ D. Geetha, geeramphyau@gmail.com | [1]Department of Physics, Annamalai University, Chidambaram, India. [2]Thiru Kolanjiappar Government Arts and Science College, Virudhachalam, Tamilnadu, India.

Recently sulfide materials have been examined as novel SC's electrode materials with enhanced electrochemical performance. The metal sulfide nanostructures such as ZnS, CuS, and CoS were utilized as electrode materials for energy storage applications [10–12]. The substitution of two or more valance states of metal constituents present in sulfides and the sulfur have high theoretical capacity than that of oxides and it can provide better capacitance behavior.

The covellite copper sulfide is exhaustively studied material attributable to great potential applications in several fields. Recently unary transition metal sulfides viz., copper cobalt sulfides [13] and iron copper sulfides [14] have been examined as new electrode materials for supercapacitor. Huang et al. synthesized CuS hexagonal nanosheets by solvothermal route and based on these CuS electrode showed a C_s of 833 Fg^{-1} under a high current density of 1 Ag^{-1} [15]. Peng et al. synthesized flower-like CuS for SCs with high C_s of 597 Fg^{-1} at a current density of Ag^{-1} [16]. Zhu et al. reported CuS nanoneedles on carbon nanotubes by a multiple step and template method, and supercapacitors via this composite demonstrated a capacitance of 114 Fg^{-1} at a scan rate of 2 mv/s in the three-electrode tests [17].

It was reported that the binary sulfides such as Zn–CuS have an electronic conductivity of about 2 orders higher than that of the oxide partners and a lot higher conductivity than that of the binary sulfides [18–20]. Also, the electrochemical commitments from both Zn and Cu ions in the binary sulfides are relied upon to give more extravagant redox responses than that of the single ternary sulfides. Pu et al. built up Zn–CuS hallow nanostructure that was sulfurized from a Zn–Cu precursor by a two-step sacrificial template method. This Zn–CuS hallow structure manifested a high C_s of 437 Fg^{-1}, when tried as a SC's material at a current density of 1 Ag^{-1} [21].

In this work, a novel mesoporous flower-like Zn–CuS and CuS nanostructure was synthesized via hydrothermal treatment using organic cationic surfactant (CTAB) as structure promoting agent. The first important point is no researcher uses flower-like mesoporous nanostructure as the electrode material to attain high C_s compared to spherical CuS nanostructure. The formation mechanism of CuS and Zn–CuS was elaborately discussed. The electrochemical behavior of the CuS and Zn–CuS was investigated as electrode material for supercapacitors in 2 M KOH electrolyte solution. As estimated, the conventional composites bear the cost of generous upgrade and prompting to enough redox reactions. Such special highlights enable the fusion electrode to display considerably enhanced energy storage ability when compared CuS and earlier reports. The results obtained from this nanocomposite demonstrated promising execution of hybrid structure of mesoporous binary metal sulfide for future energy storage applications.

The synthesis of Zn–CuS has the following aims:

1. The high electrical conductivity of Zn–CuS will assist to overcome the limited electrical conductivity
2. The Zn–CuS will relax ion transfer for the reason that the short ion diffusion paths and give reversible, quick faradic reactions.
3. The Zn–CuS will improve the utilization rates of electrode materials due to the porous nature.

The outcomes in this investigation demonstrate that the fabricated Zn–CuS show high specific capacitance, and long cycle life, and are potential electrode materials for SCs.

2 Experimental sections

2.1 Synthesis of CuS and Zn–CuS nanostructures

In a typical procedure, 1 mM of Cu $(NO_3)0.3H_2O$, 2 mM of Tu,$Sc(NH_2)_2$ and 0.1 mM of CTAB were dissolved in 40 ml of ethylene glycol and magnetic stirring for 1 h. The solution into a Teflon-lined autoclave is maintained at 140 °C for 9 h. The prepared black powder was washed many times and dried at 70 °C for 6 h. The three different concentrations of Zn–CuS were synthesized under same conditions with the addition of Zn $(NO_3)0.3H_2O$.

2.2 Materials characterization

The diffraction patterns were recorded on X'Pert-PRO using Cu Kα radiation. X-ray diffractometer was at a scan rate of 1° min^{-1} over the range 10°–70° (2θ) at room temperature. The optical properties were determined by UV–Vis spectroscopy (Shimadzu UV1700). The change in morphology on increasing the concentration of Zn-ion-doped CuS was inspected through a (JEOL-JSM – 5610 LV with INCA EDS) SEM and the elemental analysis was studied using EDX, and the morphology was confirmed with (SUPRA 55) field emission scanning electron microscope (FESEM). The TEM morphologies were analyzed on a TEM CM-200. Chemical compositions were investigated by XPS (Kratos Analytical). The BET parameters of the Zn–CuS surface area were measured in Micrometrics ASAP-2010 system using the liquid nitrogen adsorption–desorption method.

2.3 Electrochemical measurements

In our previous paper, the electrode preparation and electrochemical characterization techniques of prepared samples were discussed [22].

3 Results and discussion

3.1 XRD

The crystal phase, purity and crystallographic structures of all synthesized samples were tested by X-ray diffraction (XRD) measurements. Figure 1a depicts the XRD spectra of synthesized CuS nanostructure and Fig. 1b–d shows the synthesized Zn–CuS nanostructures. The well-crystalline diffraction patterns with 2θ values at 26.53°, 27.41°, 29.24°, 31.75°, 32.85°, 47.98°, 52.54°, and 59.05° are oriented along the (100), (101), (102), (103), (006), (110), (108), and (116) planes of covellite CuS and Zn–CuS nanostructures, with
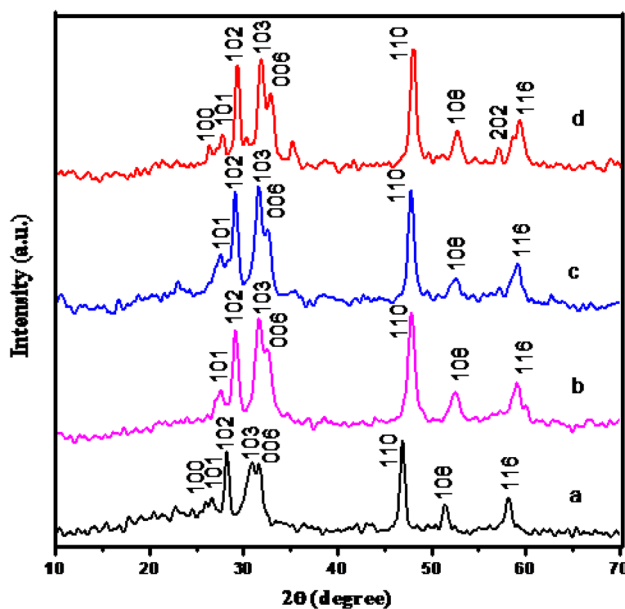

Fig. 1 XRD patterns of (0.1 mM) CTAB-assisted CuS doped with Zn: (a) 0.0, (b) 0.05, (c) 0.15 and (d) 0.30 mM

lattice constants of a = 3.792 Å and c = 16.344 Å (JCPDS No.06–0464). All diffraction planes in good crystalline quality are in good agreement with the previous report [23]. The diffraction peak of the (006) crystal plane with (0.05 mM) Zn-doped CuS is considered. This shoulder peak will be suppressed compared to pure CuS as shown in Fig. 1b. When the Zn concentration increases (0.15 mM and 0.30 mM), the (006) crystal plane also increases. Some extra peaks appear in the (0.30 mM) Zn-doped CuS. Notably, a slight left shift of the peak intensity of (0.05 mM) Zn–CuS contributes to the Zn^{2+} incorporated into CuS and the substitutional cationic sites are occupied and the peak intensity is not shifted for Zn (0.15 and 0.30 mM)-doped CuS nanostructures. These results may suggest that the Zn (0.15 and 0.30) doping concentration is appreciably incorporated into CuS lattice structure. This observation may suggest that the lower concentration of Zn^{2+} (0.05 mM) is easier to replace Cu^{2+}. Results show that (0.05 mM) Zn-doped CuS has optimum concentration as compared to other Zn (0.15 mM and 0.30 mM)-doped CuS. Absence of impurity peaks is monitored, signifying the high purity of the samples by this simple method.

The average grain sizes were found to be 14, 7, 12, and 17 nm for CuS, CuS/Zn (0.05), CuS/Zn (0.15), and CuS/Zn (0.30), respectively, and were quantified using Scherrer Eq. (1)

$$D = \frac{0.9\lambda}{\beta cos\theta} \tag{1}$$

The lattice parameters of CuS and Zn–CuS crystals are estimated using Eq. (2):

$$\frac{1}{d_{hkl}^2} = \frac{4}{3}\left(\frac{h^2 + hk + k^2}{a^2}\right) + \frac{l^2}{c^2} \tag{2}$$

For the hexagonal system, volume of the unit cell was quantified by Eq. (3) [24].

$$V = 0.8661 \times a^2 \times c \tag{3}$$

Table 1 summarizes the lattice parameters, grain size and volume of the unit cell. When dopant (Zn^{2+}) concentration increases, lattice parameters and the unit cell

Table 1 Doping concentration, lattice parameters, cell volume and average crystal size

Concentration of doping (mol%)	Lattice parameters (Å)		Cell volume Å³	Average crystal size D (nm)
	a = b	c		
(0.00%) Zn–CuS	3.789	16.345	203.213	14
(0.05%) Zn–CuS	3.791	16.352	203.514	**7**
(0.15%) Zn–CuS	3.794	16.360	203.936	12
(0.30%) Zn–CuS	3.797	16.369	203.371	17

volume increase, which reveal the well incorporation of Zn^{2+} in lattice sites.

The substitution of the Cu^{2+} ions ($r_{Cu}^{2+} = 0.74$ Å) [25] with similar radius Zn^{2+} ions ($r_{Zn}^{2+} = 0.74$ Å) [26] outcome in a minute diminish in lattice constant of CuS. But, the lattice parameters of Zn–CuS ($d_{103} = 3.791$, $d_{110} = 16.352$) are similar to that of CuS ($d_{103} = 3.789$, $d_{110} = 16.345$). It might be caused by same radii of Cu ($r_{Cu}^{2+} = 0.74$ Å) and Zn ($r_{Zn}^{2+} = 0.74$ Å). The lattice constants of the Zn–CuS are more extensively increased than the CuS nanostructures. It provides a strong confirmation for the merging of Zn^{2+} ion into the CuS lattice.

3.2 XPS

For chemical states and elemental composition of the obtained samples, X-ray photoelectron spectroscopy (XPS) measurements were conducted. Figure 2 shows the survey spectrum and the peaks recognized Zn, Cu, S, O, and C elements. The peaks for Cu, Zn, and S elements are identified in the EDS spectra (Fig. 3c, f, i, l), which confirms that the sample is generally composed Cu, Zn, and S elements. Elemental composition of the Zn–CuS is quantified by XPS, and shown in Fig. 2a. The full spectrum reveals that the survival of peaks is attributed to S, Zn, Cu, O and additionally C elements. From this survey, no other element is found which implies the high purity.

Figure 2b shows that core-level spectrum of Cu 2p is split into two main peaks Cu 2p3/2 (931.71) and Cu 2p1/2 (951.79) eV. The intensity peaks of Cu 2p3/2 and Cu 2p1/2 are separated by an energy difference of 20 eV which is fundamentally the same binding energy [27]. Figure 2c reveals the core-level spectrum of Zn 2p lines. The main peak Zn 2p3/2 appears at 1022.35 eV and another peak Zn 2p1/2 is located at 1045.23 eV [28]. In Fig. 2d, the core-level spectrum of S 2p indicates the assignment of the binding energy at 161.9 and 162.9 eV can be allocated to 2p3/2 and 2p1/2, respectively, which is typical the co-ordination of S ions with metal ions. Obviously, the XPS data demonstrate that Zn–CuS material has a composition containing S^{2+}, Zn^{2+}, and Cu^{2+}, which is consistent with the previous reference for CuS [29]. The atomic ratio of Zn, S, and Cu elements as, 1:2:1, equivalent to the chemical formula of Zn S Cu. The weight percentage and atomic percentage of Zn(0.05 mM)–CuS nanocomposite are tabulated in Table 2.
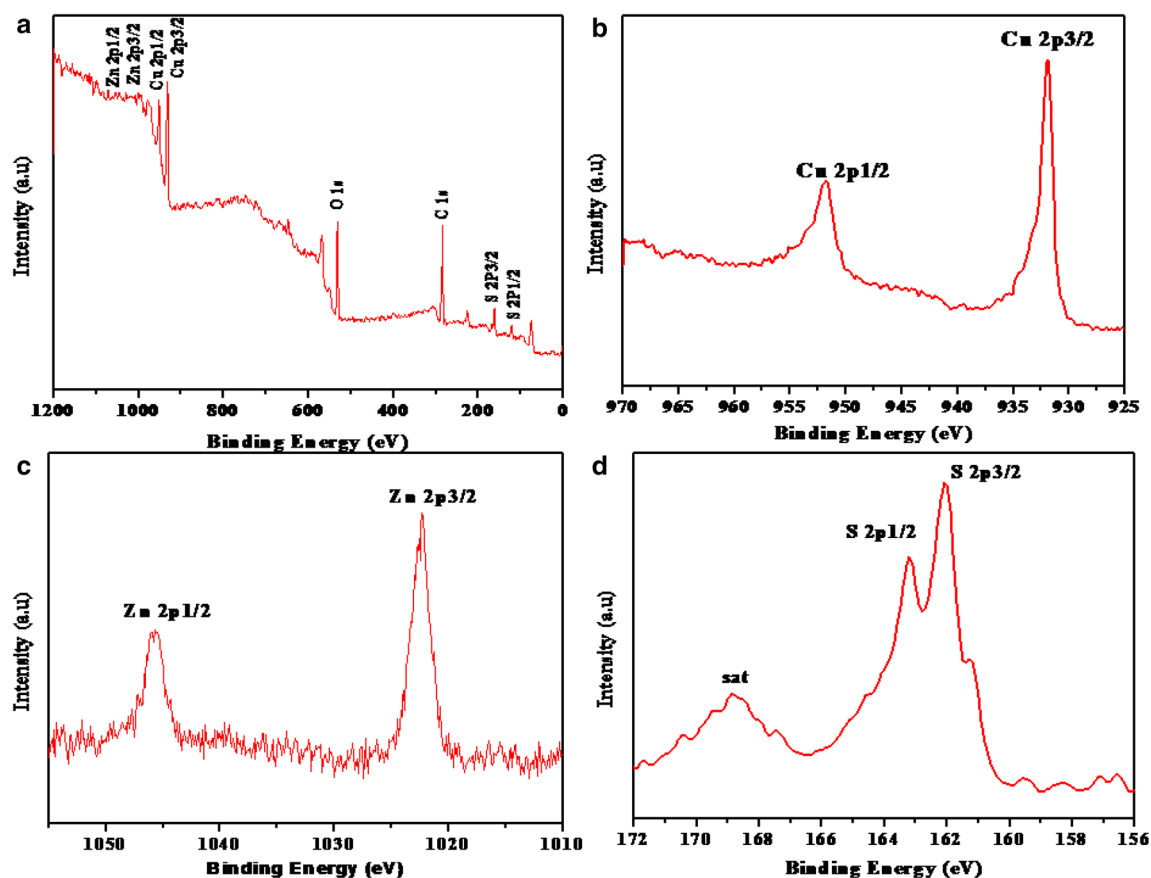

Fig. 2 XPS spectra of (0.1 mM) CTAB-stabilized Zn (0.05 mM)-doped CuS nanostructures **a** full spectrum, **b** Cu 2p, **c** Zn 2p and **d** S 2p
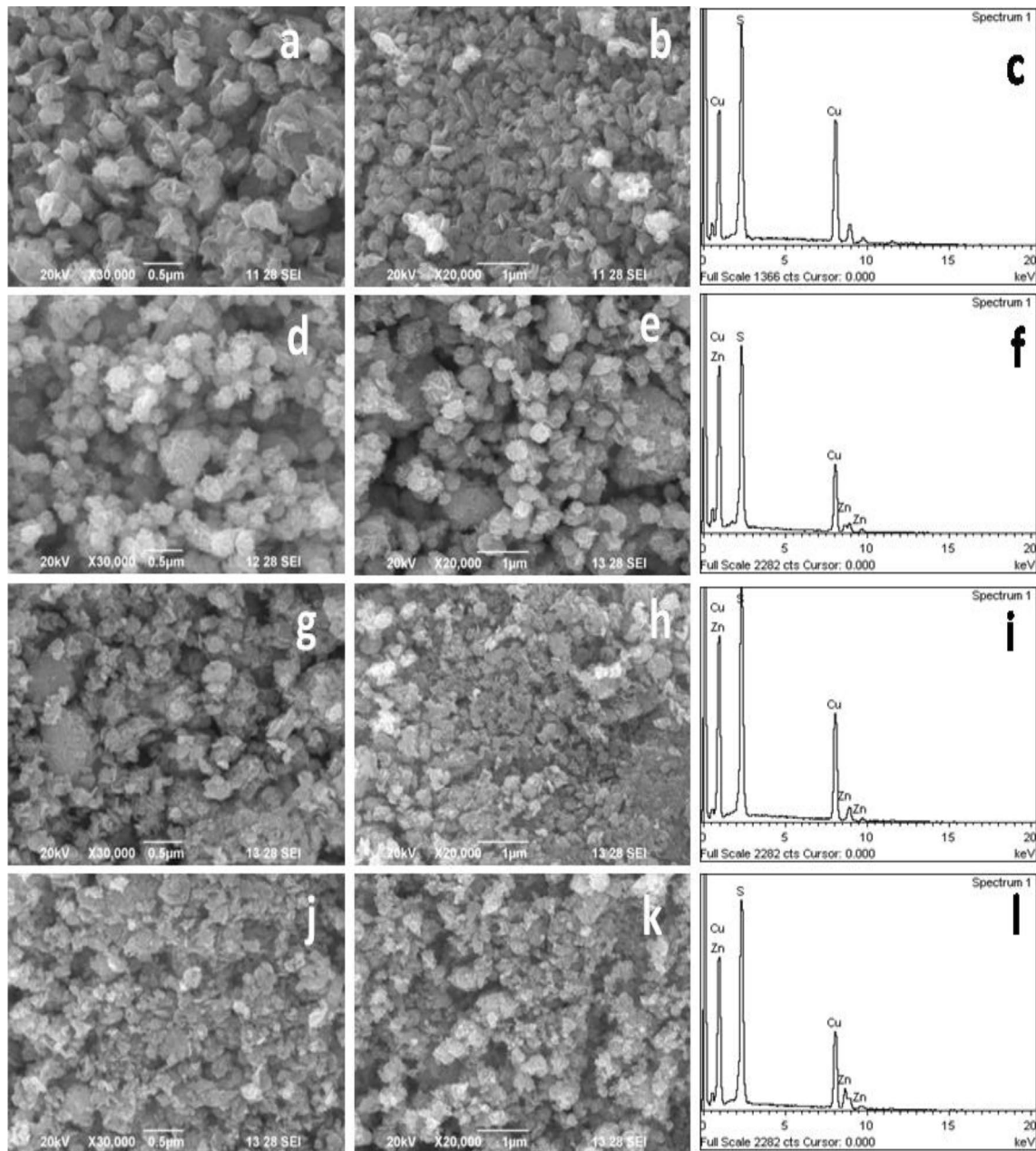
Fig. 3 SEM images of (0.1 mM) CTAB-stabilized **a**, **b** pure CuS, **d**, **e** Zn (0.05)–CuS, **g**, **h** Zn (0.15)–CuS, **j**, **k** Zn (0.30 mM)–CuS nanostructures and **c**, **f**, **i**, **l** are corresponding EDAX spectra

3.3 Surface morphological analysis

3.3.1 SEM/EDX

The representative SEM images reveal the formation of CuS and Zn–CuS structures to a size of 1 and 0.5 μm as shown in Fig. 3a–k. The SEM micrographs reveal the uniformly dispersed with cluster structure of CuS microstructures are shown in Fig. 3 (a, b). The SEM micrographs of Zn (0.05 mM)-doped CuS are shown in Fig. 3 (d, e). The flower

Table 2 Elemental analysis of Zn(0.05 mM)–CuS nanocomposite

Sample name	Element	Wt%	At%
(0.05%) Zn–CuS	C	2.1	3.11
	Cu	27.81	37.14
	S	56.73	21.27
	Zn	13.35	38.47

like structure comprises irregular nanoflakes are well defined flower like Zn doped CuS which are obtained and the regular petal growth and each microflower is arranged identical interlaced nanoflakes compared with other Zn (0.15 and 0.30)-doped CuS. The cationic surfactant is supplied as a "soft" template material to synthesize the flower-like nanostructures. The creation of transitional pores was observed on the surface, which is the specific feature for obtaining high C_s. Figure 3g, h, j, and k) depicts the remaining two samples Zn (0.15 and 0.30)–CuS micrographs which reveal irregular nanoflakes agglomerated and sheet-like accumulations are arranged and distributed zigzag patterns of the microstructures in a coherent form.

The elemental compositions were analyzed with EDX. The EDX spectra of CuS confirmed the presence of Cu and S peaks alone (Fig. 3c). The elemental compositions of Zn–CuS are shown in Fig. 3f, i and l which indicates subsistence of Cu, Zn, and S element. Absence of other elements in all the spectrums implies high purity of the samples.

3.3.2 FESEM

Figure 4a, b shows the FESEM images of Zn (0.05 mM)-doped CuS nanostructures are flower-like CuS nanostructure that is about 200 nm.

The FESEM image shows compactly combined flower urchin-like Zn (0.05 mM)–CuS architectures in the existence of CTAB. At high magnification, the image (Fig. 4b) presents each hierarchical CuS nanoflowers built up by many interleaving and slight bending nanoflakes with the thickness of about 14–20 nm, which entangle together to behave a network in the bud-like flower. The surface of the Zn–CuS appears much rough, which is essentially credited to the quick ion interactions accompanied with the Kirkendall effects amid sulfidation [30]. The rough surface has been additionally affirmed by the TEM image. The architecture might present generous upgrade in electron transport and providing active sites for redox reduction.

3.3.3 TEM/SAED

The TEM images of Zn (0.05 mM)–CuS nanostructures are flower-like morphologies in the range of 100–500 nm are shown in Fig. 4c–e. TEM images show that each nanoflower surface and outer nanostructure consists of the aggregations of darker secondary branches (nanoflakes). Moreover, these nanoflakes are interconnected to form a flower-like porous architecture. A clear dissimilarity among the pale center and dark edges can be observed, which confirms CuS nanoflowers have a hollow interior.
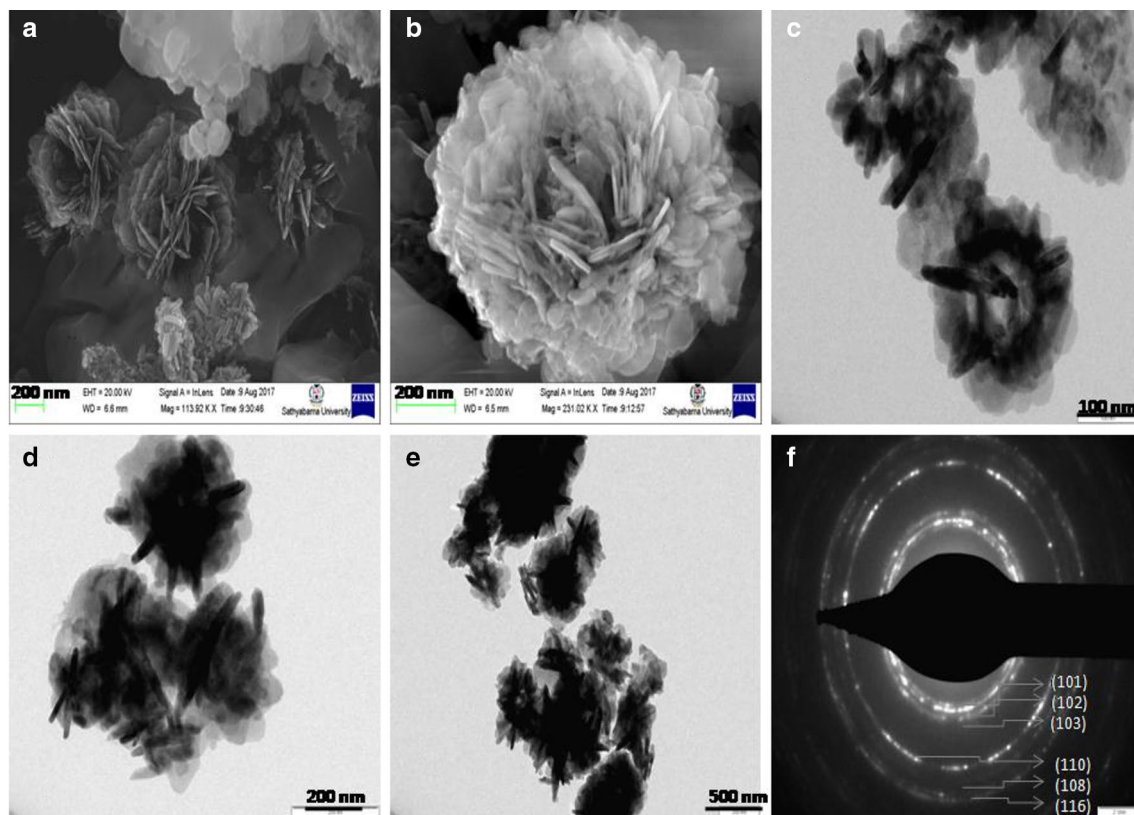

Fig. 4 a, b FESEM images **c–e** TEM images and **f** SAED pattern of (0.1 mM) CTAB-stabilized Zn (0.05 mM)-doped CuS nanostructures

There are many nanopores on the shell of the hierarchical nanostructures.

The SAED pattern (Fig. 4f) reveals well-recognized diffraction rings of Zn (0.30)–CuS representing highly structured subunits and polycrystalline nature. The SAED patterns display a set of diffraction rings which can be indexed as (101), (102), (103), (110), (108), and (116) corresponding to the Zn–CuS phase. Actually Zn (0.05 mM)–CuS signifies its crystal structure.

3.3.4 Growth mechanism

To know the growth mechanism, the reaction conditions are monitored. The SEM images demonstrate that the shape and size of the material change gradually with Zn^{2+} concentration. Based on the results obtained above, the growth mechanism of the flower-like Zn-doped CuS architectures are presented in Scheme 1.

The CTAB served as template for the formation of microstructures and thiourea serves as a sulfur source, which combines with Cu^{2+} and ethylene glycol. Initially Cu^{2+} is coordinated with Zn^{2+}, leading to the formation of metallic complexes. Hydrolysis takes place and leads to the formation of Zn and CuS nuclei when heating the solution and it contains a large number of dangling bonds and favors the introducing of Zn^{2+} to the CuS crystalline and leads to its anisotropic growth. As the reaction continues, the nanoflakes self-assembled to the hierarchical flower-like mesoporous microstructures are formed.

3.4 Optical properties

The semiconducting materials are highly dependent on the nature and it is well known that structure sensitive and the quantity of limitations are present in a crystal. Figure 5a–d depicts the UV–Vis spectra of samples CuS and Zn–CuS in the range of 200–800 nm.

The UV–Vis spectra depend on the nature of dopant concentration as well as copper and sulfur composition of CuS nanostructures. All the absorption curves appeared at 270 nm for CuS and 272, 271, 270 nm for Zn–CuS nanostructures [31] are compared with bulk CuS [32]. Especially Zn (0.05 mM)–CuS a broad absorption at 500 nm is due to the covellite phase [33] which reveals that there are distinct red shifts compared with other Zn–CuS [34, 35]. This clearly shows that the absorption edges are red shifted. The maximum red shift of the Zn–CuS nanostructures may be associated with the construction of CuS nanoflakes and it signifies decrease in the crystallite size and change in shape (nanoflowers) obtained. The ionic radius of Zn^{2+} is similar to Cu^{2+}, which indicates Zn^{2+} ion doped in CuS lattice. The unusual phenomena in the UV–Vis spectra may have many applications in the optical field.

Figure 6 shows the bandgap plots of $(\alpha h\nu)^2$ vs. $h\nu$ as per Tauc's equation for all the samples and bandgaps are 2.65, 3.60, 2.82, and 3.50 eV for CuS and Zn–CuS nanostructures, respectively. The bandgap energy values of
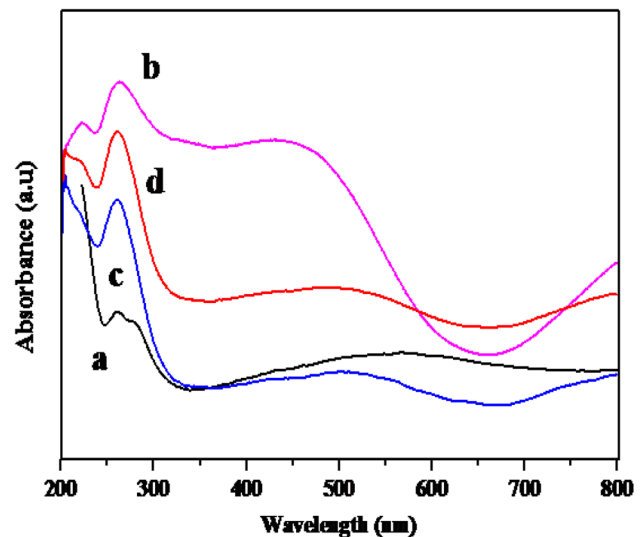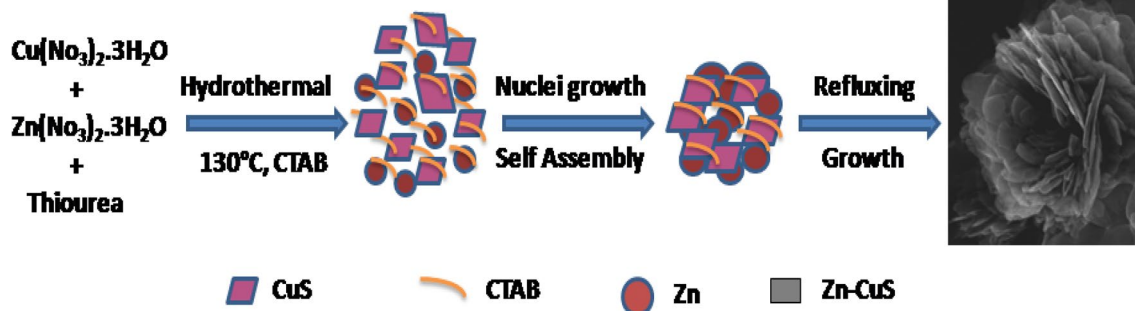

Fig. 5 UV–Vis spectra of (0.1 mM) CTAB-stabilized CuS doped with Zn: (a) 0.0, (b) 0.05, (c) 0.15 and (d) 0.30 mM

Scheme 1 Illustration of possible growth process of the flower-like Zn–CuS architectures
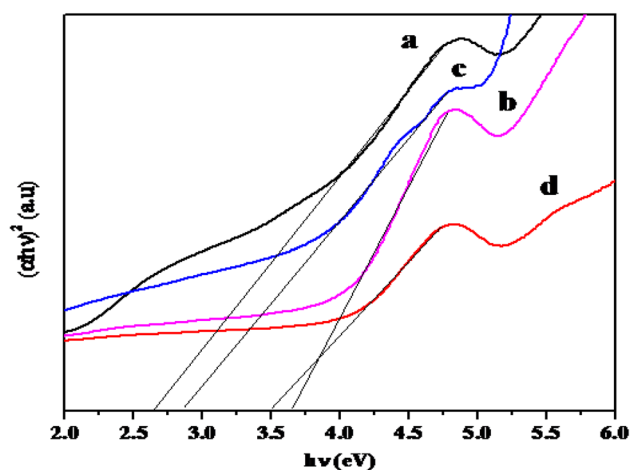
Fig. 6 Typical Tauc's plot of (0.1 mM) CTAB-stabilized CuS doped with Zn: (a) 0.0, (b) 0.05, (c) 0.15 and (d) 0.30 mM

synthesized samples are estimated [36] by the following Eq. (4):

$$(\alpha h\nu)^n = K(h\nu - E_g) \tag{4}$$

The highest absorption curve is detected at Zn (0.05 mM)–CuS (Fig. 5b) which has excellent optical property, as a result of good agreement with Zn (0.05 mM)–CuS, which is supported by XRD pattern (Fig. 1b).

3.5 BET measurements

The porous structure and specific surface area of the as-synthesized CuS and Zn (0.05 mM)–CuS nanoflowers are investigated using N_2 adsorption–desorption isotherm and the consequent results are shown in Fig. 7a, b. The hysteresis circles at a general weight of 0.3–1.1 shows that the isotherms can be assigned sort IV, and the ordinary isotherm bend watched Zn–CuS exhibited the mesoporous qualities of the anode [37]. The normal pore diameter of Zn–CuS nanofower is – 3–71 nm and for (0.1 mM) CTAB–CuS is – 3–76 nm. The surface area of the Zn–CuS is 18.23 m^2/g and for (0.1 mM) CTAB–CuS is 8.32m^2/g.

However, at high relative pressure from 0.95 to 1.0, the uptake is attributed to the pore spaces between the nanoflowers. The porous structure and high surface area provide low-resistance pathways and more electroactive sites are beneficial for the Zn–CuS, which enhances charge transport and power capability. Therefore, the Zn–CuS sample utilized as electrode materials can expect better electrochemical properties for supercapacitors.
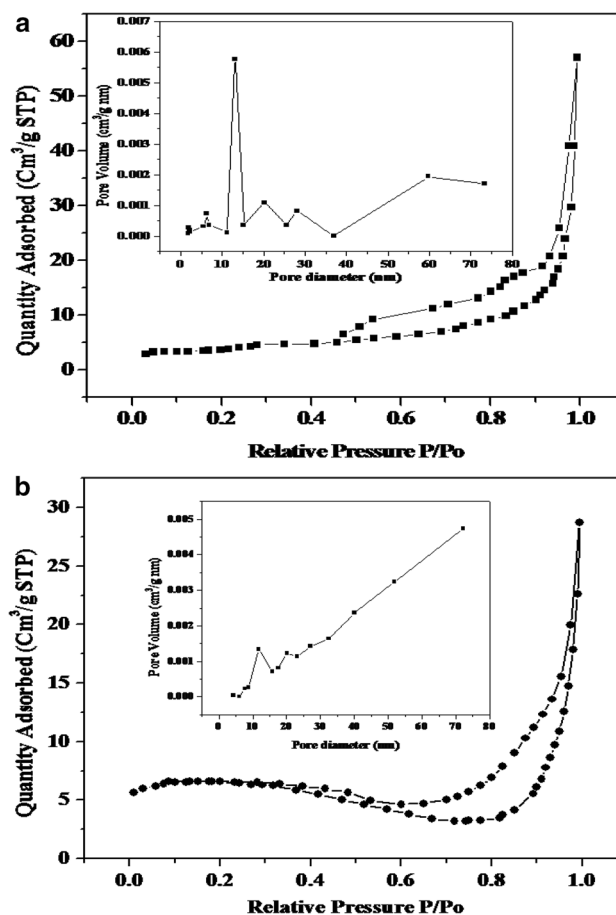

Fig. 7 a N2 adsorption–desorption analysis of (0.1 mM) CTAB-stabilized CuS nanostructures and inset represents the corresponding pore-size distribution. **b** N2 adsorption–desorption analysis of (0.1 mM) CTAB-stabilized Zn (0.05 mM)-doped CuS nanostructures and inset represents the corresponding pore

3.6 Electrochemical studies

3.6.1 Effect of scan rate

For electrochemical measurements, the as-prepared CuS and Zn–CuS nanostructures were fabricated as incorporated electrodes and explored in the three-electrode test in a voltage window between 0.0 to 0.5 V (vs. SCE) with 2 M KOH as aqueous electrolyte solution. However, Fig. 8a shows the CV curve of the CuS electrode [22] which exhibits roughly rectangular shape with weak redox curves with broad faradaic curve in the range of 0.12 to 0.41 V [38]. We assumed that the intimate bonding of CuS electrode reduced the contact resistance among them; thus, Faraday processes of the electrochemically active species become easy [39]. Figure 8b shows the redox peaks present in Zn–CuS electrode at all sweep rates which may supply fast transport and facile accessibility to active sites for electrolyte species.

Fig. 8 Electrochemical characterization of the two modified electrodes **a** CV curves of the CTAB–CuS, **b** CTAB–Zn (0.05 mM)-doped CuS electrode at various scan rates, **c** charge–discharge curve of the CTAB–CuS, **d** CTAB–Zn (0.05 mM)-doped CuS electrode at a constant current density
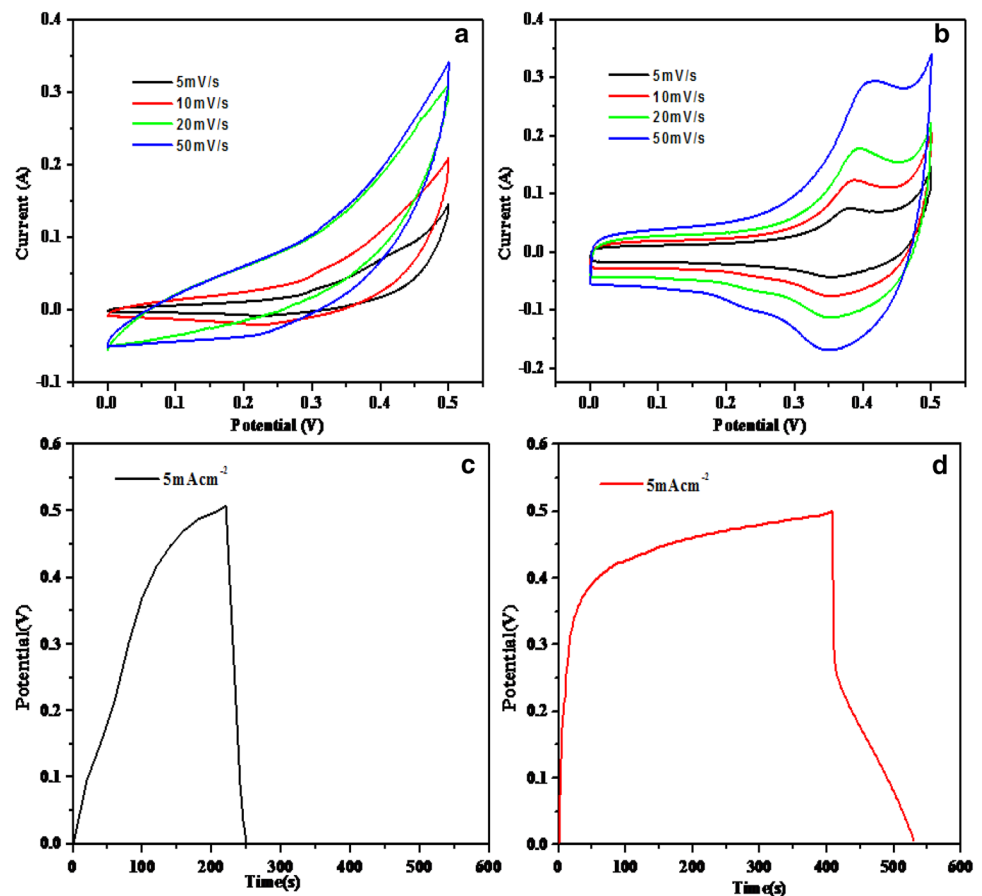
With an increasing sweep rate, a pair of redox curves was observed and better response relationship of the specific current of redox peak and a typical pseudocapacitance become visible in all the CV curves caused by Faradaic reactions inside the electrode materials [40]. It is notable that the Zn–CuS displays more positive cathodic peak potential than the CuS electrode which suggests their excellent intrinsic electrochemical ability and conductivity of the Zn–CuS electrode. At high scan rate, the CV curve has a larger area compared to the lower scan rate and resulted the capacitance decrease during the redox process [41]. Contrasted to CuS, the curve of Zn–CuS CV shows more clear redox curves and larger region, which implies better reversibility and higher capacitance in light of the fact that the electroconductibility of Zn–CuS is superior to that of CuS.

Notably the CV curves show non-rectangular shape, and Zn–CuS electrode exhibits a pseudocapacitance behavior due to Faradaic reactions which are liable for charge storage. At high scan rate, broader redox curves are obtained in Zn–CuS CV than the low scan rate. When compared with the CTAB–CuS electrode, the CTAB–Zn-doped CuS electrode exhibits a greater area of CV curves, indicating the CTAB/Zn–CuS electrodes acquire higher C_s. The smallest

variations in redox curve positions indicate low polarization effect which may feature the difference in electrode polarization behaviors. This behavior is closely related to the chemical composition and physical morphology of the electrode material. This excellent C_s may be ascribed to the mesoporous structure of Zn–CuS. Porous structure can be considered to get better consumption and the C_s of electroactive materials [42].

3.6.2 Chronopotentiometry test

The chronopotentiometric measurements were done to quantify the C_s of CuS and Zn–CuS materials. Figure 8c, d illustrates GCD curves of two electrodes at a current density of 5 mA cm^{-1} signifying the Faradaic reaction. Obviously, the discharge curve can be separated into two districts, a rapid potential fall caused by the internal resistance of electrode materials and a time-consuming potential decay owing to the Faradic redox reaction. The C_s of both CuS and Zn–CuS electrodes is determined from the discharge curves according to the following Eq. (5): [43, 44]

$$Cs = \frac{I\Delta t}{m\Delta V} \qquad (5)$$

The CTAB/CuS modified GCE delivers 328.26 Fg^{-1} at 5 mA cm^{-2} and the CTAB/Zn–CuS modified GCE delivers 826.31 Fg^{-1} at 5 mA cm^{-2}. C_s of the CTAB/Zn–CuS is higher than that of CuS electrode material. The highest C_s enhanced owing to two reasons: (1) Improved electrical conductivity provides fast charge transfer in Zn–CuS and (2) Porous structure of Zn–CuS nanostructures can considerably extend the consumption and the C_s of electroactive materials [45]. Comparison of specific capacitance for synthesized CuS and Zn–CuS electrode materials with other reported electrode materials are tabulated in Table 3.

3.6.3 EIS

Figure 9 displays the EIS results of the CuS and Zn–CuS electrodes in the fitting circuit (see inset the equivalent circuit of the supercapacitor in Fig. 9), R_s is solution resistance and R_{ct} is charge transfer resistance, C_{dl} is the double layer capacitance and Z_w is the Warburg impedance.

Nyquist plot of CuS and Zn–CuS electrodes is shown in Fig. 9a, b. In samples (a and b), at high-frequency region a semicircle is obtained and goes to (R_{ct}) of the electrode. This R_{ct} is mostly relay to the surface region of the Zn–CuS, because of the Faradic process of CuS and Zn–CuS. Both electrodes exhibit a linear portion in the lower frequency region and semicircle in the high-frequency region corresponding to Warburg impedance (Z_w) [46]. Both the materials have ideal capacitor behavior. Also the electrochemical impedance spectra analyzed by nyquist plot confirmed by capacitance behavior. The current study diameter of the semicircle for CTAB/CuS increases as compared with Zn–CuS. From this EIS analysis, Zn–CuS electrode exposes suitable electrode for SCs.
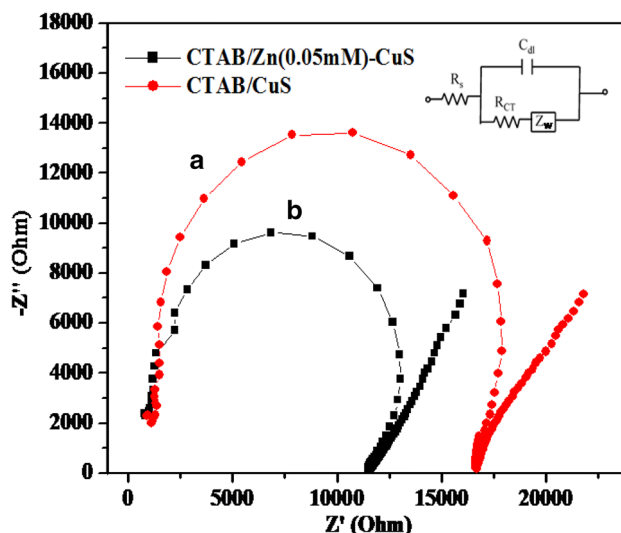

Fig. 9 (a) EIS spectra of the CTAB–CuS, (b) CTAB–Zn (0.05 mM)-doped CuS electrode

4 Highlights

- Development of new useful Zn–CuS nanocomposites electrode materials for supercapacitor will be the outcome of this paper.
- Porous nature of Zn–CuS nanocomposites will play major role can provide fast ion/ electron transfer leads to improved reaction kinetics and high performance compared to other hybrid composites. The mesopores in these materials can supply numerous catalytically active sites, facilitating the oxygen diffusion and electrolyte throughout the electrode.
- Major drawback of supercapacitor is low energy density compared to batteries. To overcome this draw back by changing suitable electrode material, this may enhance the energy density and stability of the supercapacitors in future.
- Therefore, it is extremely important to develop alternative metal sulfide electrode material with a combination of low cost, larger capacitance and excellent electrochemical stability.
- Combining all the above results, it has been concluded that the Zn–CuS nanocomposites used in the present work proves to be a low cost and environment friendly in nature for its application as an electrode materials in supercapacitors.

Table 3 Comparison of specific capacitance for synthesized CuS and Zn–CuS electrode materials with other reported electrode materials

Electrode materials	Specific capacitance (Fg^{-1})	Reference
GNPs	312 @ 20 mV s^{-1}	Aval et al. (2018) [47]
PVA/KOH	922 @ 2 mA/cm^2	Fard et al. (2019) [48]
CNTs	410 @ 20 mV s^{-1}	Aval et al. (2018) [49]
CuS	328 @ 5 mA/cm^2	Present work
Zn–CuS	826 @ 5 mA/cm^2	Present work

5 Conclusion

In summary, a novel hierarchical Zn–CuS mesoporous nanoflowers are synthesized by simple one-pot mild hydrothermal approach. The crystal phase, purity and grain size are estimated by XRD. The SEM, FESEM and TEM images of Zn–CuS show that flower-like nanostructures are built up by many interleaving slightly bending nanoflakes. Profiting from the progressive and mesoporous structures have demonstrated considerable upgrade in active sites for redox responses. The growth mechanism is discussed elaborately. The pore diameter of Zn–CuS nanoflower is – 3–71 nm. The BET surface area of the Zn–CuS sample is 18.23 m^2/g. Moreover, the Zn–CuS samples exhibit superior specific capacitance, and the Zn^{2+} ion concentration on CuS is optimized. The electrochemical behavior of the mesoporous nanoflowers can be ascribed to the effect of these factors viz., high surface area, the presence of mesopores and the existence of nanoflakes in the flower. The existence of CTAB behaves as shape promoting and is also favorable for mesoporous structures. The Zn–CuS sample exhibits high specific capacitance 826.31 Fg^{-1} at 5 mA cm^{-2}. The consequences of supercapacitors with the Zn–CuS electrode propose that such effortless strategy holds a promising electrode for superior supercapacitors.

Compliance with ethical standards

Conflict of interest The authors declare no conflict of interest.

References

1. Hsu YK, Chen YC, Lin YG (2014) Synthesis of copper sulfide nanowire arrays for high-performance supercapacitors. Electrochim Acta 139:401–407
2. Heydari H, Moosavifard SE, Elyasi S, Shahraki M (2017) Nanoporous CuS nano-hollow spheres as advanced material for high-performance supercapacitors. Appl Surf Sci 394:425–430
3. Peng H, Ma G, Mu J, Sun K, Lei Z (2014) Controllable synthesis of CuS with hierarchical structures via a surfactant-free method for high-performance supercapacitors. Mater Lett 122:25–28
4. He D, Wang G, Liu G, Bai J, Suo H, Zhao C (2017) Facile route to achieve mesoporous $Cu(OH)_2$ nanorods on copper foam for high-performance supercapacitor electrode. J Alloy Compd 699:706–712
5. Krishnamoorthy K, Veerasubramani GK, Pazhamalai P, Kim SJ (2016) Designing two dimensional nanoarchitectured MoS_2 sheets grown on Mo foil as a binder free electrode for supercapacitors. Electrochim Acta 190:305–312
6. Simon P, Gogotsi Y (2008) Materials for electrochemical capacitors. Nat Mater 7:845
7. Peng S, Li L, Tan H, Cai R, Shi W, Li C, Mhaisalkar SG, Srinivasan M, Ramakrishna S, Yan Q (2014) Hollow spheres: MS_2 (M = Co and Ni) hollow spheres with tunable interiors for high-performance supercapacitors and photovoltaics. Adv Funct Mater 24:2155
8. Xia X, Zhu C, Luo J, Zeng Z, Guan C, Ng CF, Zhang H, Fan HJ (2014) Synthesis of free-standing metal sulfide nanoarrays via anion exchange reaction and their electrochemical energy storage application. Small 10:766
9. Xiao J, Wan L, Yang S, Xiao F, Wang S (2014) Design hierarchical electrodes with highly conductive $nico_2s_4$ nanotube arrays grown on carbon fiber paper for high-performance pseudocapacitors. Nano Lett 14:831
10. Jayalakshmi M, Rao MM (2006) Synthesis of zinc sulphide nanoparticles by thiourea hydrolysis and their characterization for electrochemical capacitor applications. J Power Sources 157:624–629
11. Tsamouras D, Kobotiatis L, Dalas E, Sakkopoulos S (1999) An impedance study of the metal sulfide $Cu_xZn_{(1−x)}S$ electrolyte interface. J Electroanal Chem 469:43–47
12. Wang B, Park J, Su D, Wang C, Ahn H, Wang G (2012) Solvothermal synthesis of CoS_2–graphene nanocomposite material for high-performance supercapacitors. J Mater Chem 22:15750–15756
13. Moosavifard SE, Fani S, Rahmanian M (2016) Hierarchical CuCo2S4 hollow nanoneedle arrays as novel binder- free electrodes for high-performance asymmetric supercapacitors. Chem Commun 52:4517–4520
14. Pei LZ, Wang JF, Tao XX, Wang SB, Dong YP, Fan CG, Zhang Q-F (2011) Synthesis of CuS and $Cu_{1.1}Fe_{1.1}S_2$ crystals and their electrochemical properties. Mater Charact 62:354–359
15. Huang K-J, Zhang J-Z, Fan Y (2015) One-step solvothermal synthesis of different morphologies CuS nanosheets compared as supercapacitor electrode materials. J Alloys Compd 625:158–163
16. Peng H, Ma G, Jingjing Mu, Sun K, Lei Z (2014) Controllable synthesis of CuS with hierarchical structures via a surfactant-free method for high-performance supercapacitors. Mater Lett 122:25–28
17. Zhu T, Xia B, Zhou L, Lou XWD (2012) Arrays of ultrafine CuS nanoneedles supported on a CNT backbone for application in supercapacitors. J Mater Chem 22:7851
18. Wang X, Liu WS, Lu X, Lee PS (2012) Dodecyl sulfate induced fast faradic process in nickel cobalt oxide/reduced graphite oxide composite material and its application for asymmetric supercapacitor device. J Mater Chem 22:23114
19. Ding R, Qia L, Jia M, Wang H (2013) Facile and large-scale chemical synthesis of highly porous secondary submicron/micron-sized $NiCo_2O_4$ materials for high-performance aqueous hybrid AC-$NiCo_2O_4$ electrochemical capacitors. Electrochim Acta 107:494
20. Tang C, Tang Z, Gong H (2012) J Electrochem Soc 159:A651
21. Pu J, Cui FL, Chu SB, Wang TT, Sheng EH, Wang ZH (2014) ACS Sustainable Chem Eng 2:809–815
22. Surekha P, Geetha D, Ramesh PS (2017) One-pot synthesis of CTAB stabilized mesoporous cobalt doped CuS nano flower with enhanced pseudocapacitive behavior. J Mater Sci: Mater Electron 28:15387–15397
23. Du H, Jiao L, Cao K, Wang Y, Yuan H (2013) Polyol-mediated synthesis of mesoporous α-Ni $(OH)_2$ with enhanced supercapacitance. Appl Mater Interfaces 5:6643
24. Gandhi V, Ganesan R, Syedahamed AHH, Thaiyan M (2014) Effect of cobalt doping on structural, optical, and magnetic properties of ZnO nanoparticles synthesized by coprecipitation method. J Phys Chem C 118:9715–9725

25. Shannan RD (1976) Revised effective ionic radii and systematic studies of interatomic distances in halides and chalcogenides. Acta Crystallogr A 32:751

26. Wang P, Gao Y, Li P, Zhang X, Niu H, Zheng Z (2016) Doping Zn2+ in CuS nanoflowers into chemically homogeneous $Zn_{0.49}Cu_{0.50}S_{1.01}$ superlattice crystal structure as high-efficiency n-type photoelectric semiconductors. Appl. Mater. Interfaces. 8:15820–15827

27. Feng X, Li Y, Liu H, Li Y, Cui S, Wang N, Jiang L, Liu X, Yuan M (2007) Controlled growth and field emission properties of CuS nanowalls. Nanotechnology 18:145706

28. Xiao Y, Lei Y, Zheng B, Gu L, Wang Y, Xiao D (2015) Rapid microwave-assisted fabrication of 3D cauliflower-like $NiCo_2S_4$ architectures for asymmetric supercapacitors. RSC Adv 5:21604

29. Tanveer M, Cao C, Ali Z, Aslam I, Idrees F, Khan WS, But FK, Tahira M, Mahmood N (2014) Template free synthesis of CuS nanosheet-based hierarchical microspheres: an efficient natural light driven photocatalyst. Cryst Eng Comm 16:5290

30. Yang J et al (2014) Electrochemical performances investigation of NiS/rGO composite as electrode material for supercapacitors. Nano Energy 5:74–81

31. Chen C, Li Q, Wang Y, Li Y, Zhong X (2011) Room temperature synthesis of flower-like CuS nanostructures under assistance of ionic liquid. Front Optoelectron China 4:150–155

32. Xu H, Wang W, Zhu W, Zhou L (2006) Synthesis of octahedral CuS nanocages via a solid–liquid reaction. Nanotechnology 17:3649–3654

33. Silvester EJ, Grieser F, Sexton BA, Healy TW (1991) Spectroscopic studies on copper sulfide sols. Longmuir 7:2917

34. Gao J, Li Q, Zhao H, Li L, Liu C, Gong Q, Qi L (2008) One-pot synthesis of uniform Cu_2O and CuS hollow spheres and their optical limiting properties. Chem Mater 20:6263–6269

35. Haram SK, Mahadeshwar AR, Dixit SG (1996) Synthesis and characterization of copper sulfide nanoparticles in triton-X 100 water-in-oil microemulsions. J Phys Chem 100:5868–5873

36. Pankove JI (1971) Optical processes in semiconductors. Prentice-Hall, Englewood Cliffs, NJ

37. Song K, Song WL, Fan LZ (2015) Scalable fabrication of exceptional 3D carbon networks for Supercapacitors. J Mater Chem A 3:16104–16111

38. Silambarasan M, Ramesh PS, Geetha D, Venkatachalam V (2016) A report on 1D $MgCo_2O_4$ with enhanced structural, morphological and electrochemical properties. J Mater Sci: Mater Electron 28:6880–6888

39. Fang Y, Luo B, Jia Y, Li X, Wang B, Song Q, Kang F, Zhi L (2012) Renewing functionalized graphene as electrodes for high-performance supercapacitors. Adv Mater 24:6348–6355

40. Yang J, Guo W, Li D, Qin Q, Zhang J, Wei C, Fan H, Wu L, Zheng W (2014) Hierarchical porous $NiCo_2S_4$ hexagonal plates: formation via chemical conversion and application in high performance supercapacitors. Electrochimi Acta 144:16–21

41. Silambarasan M, Ramesh PS, Geetha D (2016) Facile one step synthesis structural, optical and electrochemical properties of $NiCo_2O_4$ nanostructure. J Mater Sci: Mater Electron 28:323–336

42. Surekha P, Geetha D, Ramesh PS (2017) Preparation and characterization of porous hollow sphere of Ni doped CuS nanostructures for electrochemical supercapacitor electrode material. Springer Proc Phys 189:277–288

43. Behzadi PG, Fekri AL, Mirzaee M (2018) Flexible graphene supercapacitor based on the PVA electrolyte and $aTiO_3$/ PEDOT:PSS composite separator. J Mater Sci: Mater Electron 29:17432–17437

44. Mirzaee M, Pour GB (2018) Design and fabrication of Ultracapacitor based on paper substrate and $BaTiO_3$/PEDOT: PSS separator film. Recent Patent Nanotechnol 12(3):192–199

45. Silambarasan M, Padmanathan N, Ramesh PS, Geetha D (2016) Spinel $CuCo_2O_4$ nanoparticles: facile one-step synthesis, optical, and electrochemical properties. Mater Res Express 3(9):1–11

46. Silambarasan M, Ramesh PS, Geetha D (2017) Co-precipitation synthesis and enhanced electrochemical pseudocapacitive properties of spinel nickel cobaltite nanostructures modified glassy carbon electrodes. Springer Proc Phys 189:219–231

47. Fekri AL, Ghoranneviss M, Behzadi PG (2018) Graphite nanoparticles paper supercapacitor based on gel electrolyte. Mater Renew Sustain Energy 7:29

48. Nazarpour FH, Behzadi PG, Nasiri SM, Esmaili P (2019) PVA-based supercapacitors. Int J Ion Sci Technol Ion Motion 25(7):2951–2963

49. Fekri AL, Ghoranneviss M, Pour BG (2018) Highperformance supercapacitors based on the carbon nanotubes, graphene and graphite nanoparticles electrodes. Heliyon 4:e00862